Q. J. R. Meteorol. Soc. (2006), **132**, pp. 383–403 doi: 10.1256/qj.05.50

Vertically integrated sensible-heat budgets for stable nocturnal boundary layers

By REINA NAKAMURA* and L. MAHRT†
Oregon State University, USA

(Received 23 March 2005; revised 11 August 2005)

SUMMARY

The stable nocturnal boundary layer is commonly viewed or modelled as a balance between the temperature tendency (cooling) and vertical heat-flux divergence. Sometimes the radiative-flux divergence is also included. This perspective has dictated the design of field experiments for investigating stable nocturnal boundary layers.

Tower-based micrometeorological data from three field campaigns are analysed to evaluate the vertically integrated sensible-heat budget for nocturnal stable conditions. Our analysis indicates frequent occurrence of large imbalance between the temperature tendency and vertical heat-flux divergence terms. The values of the radiative-flux divergence are generally too small and sometimes of the wrong sign to explain the residual. An analysis of random flux errors and uncertainties in the tendency term indicate that such errors cannot explain large imbalances, suggesting the importance of advection of temperature or possibly the divergence of mesoscale fluxes. The implied role of advection is consistent with circumstantial evidence. Even weak surface heterogeneity can create significant horizontal gradients in stable boundary layers. However, it is shown that existing field data and observational strategy do not allow adequate evaluation of advection and mesoscale flux divergence terms.

KEYWORDS: Advection Mesoscale transport

1. INTRODUCTION

Physical processes contributing to evolution of stable boundary layers have been normally examined with a one-dimensional approach. Shear-generated turbulence transfers heat downwards to the cooled surface, leading to development of an inversion layer where the cooling is due to vertical divergence of the turbulent heat flux. A few studies (e.g. Brunt 1939; Anfossi *et al.* 1976) have explained the evolution of surface inversions based on the vertical radiative-flux divergence. In other studies, both vertical radiative- and heat-flux divergence are taken into account for evolution of stable boundary layers (Nieuwstadt 1980; André and Mahrt 1982). However, most studies have assumed that local cooling is driven only by the vertical heat-flux divergence.

The one-dimensional approach, which assumes that temperature advection is negligible, has dominated the design of field experiments for investigating stable boundary layers, and reliable estimates of temperature advection have not been made. Traditional stable boundary layers were studied with the assumption of flat homogeneous terrain (e.g. Brost and Wyngaard 1978; Caughey *et al.* 1979; Nieuwstadt 1984; Troen and Mahrt 1986), and the assumption of a well-defined boundary-layer top (Nieuwstadt 1984; Holtslag and Nieuwstadt, 1986).

In recent years, the concept of the nocturnal stable boundary layer has changed significantly with more extensive observations. Some aspects have been summarized in Van de Wiel *et al.* (2002). With sufficient stability, the turbulence may become highly intermittent (Howell and Sun 1999; Moraes *et al.* 2004; Salmond 2005) and the characteristics of such intermittency vary spatially even over surfaces that would be considered relatively homogeneous for daytime convective conditions (Coulter and Doran 2002; Nakamura and Mahrt 2005a). Elevated turbulence can be generated by shear associated with low-level jets (Smedman 1988; Cuxart *et al.* 2000; Banta *et al.* 2002; Lundquist 2003) and gravity waves (Forrer and Rotach 1997; Chimonas 1999),

* Present affiliation: Forestry and Forest Products Research Institute, Tsukuba, Ibaraki, Japan.
† Corresponding author: College of Oceanic and Atmospheric Sciences, Oregon State University, Corvallis, OR 97331, USA. e-mail: mahrt@coas.oregonstate.edu
© Royal Meteorological Society, 2006.

or triggered by passage of density currents (Sun *et al.* 2002). As a result, the turbulence variances and fluxes often increase with height above the surface so that a surface-based nocturnal boundary layer is difficult to define (Vickers and Mahrt 2004).

In strongly stratified boundary layers, turbulent motions close to the surface can become extremely weak for extended periods. Turbulent transport between the surface and the atmosphere ceases, sometimes referred to as 'crashing' (Derbyshire 1999). Van de Wiel *et al.* (2002) identifies this flow regime as a 'radiative regime'. Both of these studies elucidate the flow regimes in relation to dynamic stability, as related to surface radiative forcing, the horizontal pressure gradient, thermal properties of the surface and surface roughness.

The above studies suggest that evaluation of the heat budget of the nocturnal boundary layer is limited by the frequent inability to define the depth of the boundary layer. In this study, we evaluate the heat budget for layers defined by the vertical extent of the towers. The primary goals are: (i) to investigate the validity of the one-dimensional heat budget from three field programs over weak surface heterogeneity; (ii) to examine factors contributing to the difficulties in closing the layer heat budget.

The symbols used in this paper are defined in appendix D.

2. Sensible-heat budget equation

The relative importance of each term in the heat budget depends on the choice of averaging time and decomposition technique. Difficulties with consistency arise when trying to evaluate both flux divergence and temperature tendency terms. Turbulence is theoretically described in terms of ensemble averages for random processes and associated Reynolds averaging. An arbitrary variable, ϕ, is decomposed as

$$\phi = \phi' + [\phi], \tag{1}$$

where ϕ' is the turbulence fluctuation and $[\phi]$ is the ensemble average of ϕ over all of the realizations. The sensible-heat budget can then be written as

$$\frac{\partial[\theta]}{\partial t} = -[\mathbf{V}_{\mathrm{H}}]\cdot\nabla[\theta] - [\mathbf{W}]\frac{\partial[\theta]}{\partial z} - \frac{\partial[u'\theta']}{\partial x} - \frac{\partial[v'\theta']}{\partial y} - \frac{\partial[w'\theta']}{\partial z} - \frac{1}{\rho c_p}\frac{\partial[F_n]}{\partial z}, \tag{2}$$

where phase change of water vapour is neglected. The ensemble-averaging operator [ ] may be a function of space and time relative to the beginning of the realizations. From the left, individual terms represent the local or Eulerian time derivative, hereafter referred to as temperature tendency, horizontal advection, vertical advection, heat-flux divergence in the along-wind direction, heat-flux divergence in the cross-wind direction, vertical heat-flux divergence, and radiative-flux divergence.

Ensemble averages are not possible in geophysical flows. Therefore, one normally assumes that the flow is sufficiently stationary that the ensemble average can be replaced with time averaging. Spatial and temporal derivatives of the mean flow are still permitted, but are assumed to occur on much larger scales than the turbulence: that is, the flow is characterized by a spectral gap between turbulent motions and larger-scale flow.

However, the approximation of separation of time-scales is rarely realized in geophysical flows. Mesoscale motions on scales just larger than turbulence scales are normally present (e.g. Gage 1979; Lilly 1983; Mahrt *et al.* 2001a; Vickers and Mahrt 2003). Nonetheless, useful turbulence statistics can be constructed, provided that one carefully selects averaging times to define the perturbations and recognizes that non-stationarity degrades the meaning of the turbulence statistics. Then, the flow is

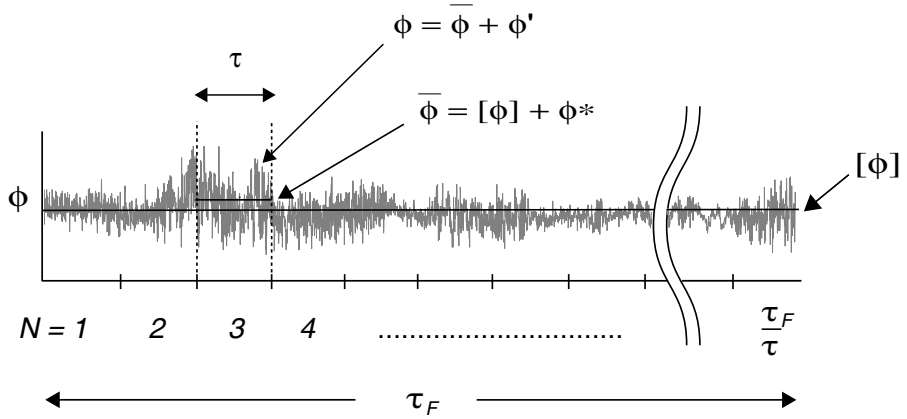

Figure 1. An example time series of ϕ of length τ_F illustrating the three-way decomposition into ϕ', ϕ^* and $[\phi]$ (see Eq. (3)). The index N indicates the position of the non-overlapping window of width τ.

decomposed as

$$\phi = \phi' + \phi^* + [\phi]. \tag{3}$$

The operator [ ] is now the time-averaging operator over time-scale τ_F which attempts to approximate an ensemble average, here chosen to be the record length; ϕ^* represents mesoscale motions on time-scales smaller than the record length but larger than turbulence time-scales (Fig. 1).

One must choose a sufficiently small averaging time τ to define turbulence motions ϕ', which excludes mesoscale motions (see section 4). Turbulence statistics such as covariances are often averaged over the longer record length τ_F, to reduce the random error. Turbulence and mesoscale fluctuations can also be written as

$$\phi' = \phi - \overline{\phi}, \tag{4}$$

$$\phi^* = \overline{\phi} - [\phi], \tag{5}$$

where $\overline{(\,)}$ is an averaging operator over the time-scale τ used to define turbulence fluctuations. In order to strictly satisfy Reynolds averaging, the time averages must be unweighted simple (block) averages.

With unweighted averaging, the vertical flux of variable ϕ averaged over a record consists of three components:

$$[w\phi] = [\overline{w'\phi'}] + [w^*\phi^*] + [[\mathbf{W}][\phi]], \tag{6}$$

where the three terms on the right-hand side are the estimate of the ensemble-averaged turbulence flux, mesoscale flux and the transport due to mesoscale and synoptic-scale motions on a scale larger than the record length (τ_F), respectively. The third term is normally converted to the advection form by applying the incompressible mass continuity equation to all three momentum equations. Equations for horizontal flux of variable ϕ can be written analogously to Eq. (6).

The heat budget equation then becomes:

$$\begin{aligned}\frac{\partial[\theta]}{\partial t} = &-[\mathbf{V}_\mathrm{H}]\cdot\nabla[\theta] - [\mathbf{W}]\frac{\partial[\theta]}{\partial z} - \frac{\partial[\overline{u'\theta'}]}{\partial x} - \frac{\partial[\overline{v'\theta'}]}{\partial y} - \frac{\partial[\overline{w'\theta'}]}{\partial z} \\ &- \frac{\partial[u^*\theta^*]}{\partial x} - \frac{\partial[v^*\theta^*]}{\partial y} - \frac{\partial[w^*\theta^*]}{\partial z} - \frac{1}{\rho c_p}\frac{\partial[F_n]}{\partial z}.\end{aligned} \tag{7}$$

Here, we assign the tendency of mesoscale temperature fluctuations $\partial[\theta^*]/\partial t$, to be zero because the expected ensemble average of θ^* is zero. Deviations of estimated $\partial[\theta^*]/\partial t$ from zero are considered as random errors.

The tendency term in Eq. (7) is not well defined in that $\partial[\theta]/\partial t = 0$ for the entire record except for the beginning and the end of the record when $\partial[\theta]/\partial t = \infty$. This is an artifact of replacing the ensemble average by the block time average. To ameliorate this problem, the temperature tendency can be estimated from the beginning and end of an individual record with a finite differencing method after smoothing the original time series of θ. This approach can be viewed as applying filtering only to the tendency term (Finnigan *et al.* 2003) and introduces formal inconsistencies in the approximation of the ensemble average of the temperature tendency and fluxes. Applying the same filter to the flux terms introduces extra Leonard eddy-covariance terms, thus additional terms in the heat budget equation, Eq. (7). Two versions of this approach are introduced in section 4(a) and compared in the appendix A. Use of instantaneous potential-temperature measurements at the beginning and end of a record for the tendency calculation leads to a poor estimate of the ensemble average since it can be strongly influenced by individual eddies.

In summary, unambiguous self-consistent estimates of the temperature tendencies and fluxes are not possible in geophysical flows because of the lack of ensemble averaging. However, more meaningful estimates of the turbulent flux are possible by carefully choosing the averaging time to define turbulence perturbations separately for each record (section 4).

3. Data

(*a*) *CASES-99*

The Cooperative Atmosphere–Surface Exchange Study-99 (CASES-99) took place over grassland in south central Kansas, USA in October 1999 (Poulos *et al.* 2002). On the 60 m main tower, wind and flux measurements were made at 6 levels (10, 20, 30, 40, 50 and 55 m) at 20 Hz by sonic anemometers (ATI K-probe and Campbell Csat3). On the same tower, thermocouples measured air temperature at 5 Hz at 32 levels with 1.8 m intervals between 2.3 and 58.1 m height. To avoid the influence of equipment at the bottom of the main tower, near-surface wind and flux measurements were made at a 10 m tower located 10 m away from the main tower. The 10 m tower was equipped with sonic anemometers at 1.5 and 5 m and thermocouples at 0.23 and 0.63 m. The sonic anemometer at 1.5 m was moved to 0.5 m towards the end of the experiment. The measurements from the 60 m tower and 10 m tower are analysed together as the main tower data in this study.

In addition, turbulence-flux measurements were made at 5 m levels by sonic anemometers on two sets of three satellite towers surrounding the main tower, situated on circles of 100 and 300 m radius, respectively. We discard all sonic anemometer data collected between the wind directions of 202° and 337° to avoid flow through the towers.

(*b*) *FLOSSII*

Fluxes over Snow Surfaces II (FLOSSII) was conducted over grassland in northern Colorado, USA from November 2002 to April 2003 (Mahrt and Vickers 2005). Sonic anemometers (Campbell Csat3) were operated at 50 Hz at 1, 2, 5, 10, 15, 20 and 30 m on a 34 m tower. Aspirated thermistors monitored air temperature at 1 Hz at the same heights as the sonic anemometers. The grass was often partially or fully covered

TABLE 1. SUMMARY OF AIR LAYERS CONSIDERED FOR HEAT BUDGET ANALYSIS

Field experiment	Layer bottom (m)	Layer top (m)	Temperature measurement heights (m)
CASES-99 (lower)	5	20	5.9, 7.2, 9.5, 11.3, 13.1, 14.9, 16.7, 18.5 (thermocouples)
CASES-99 (upper)	30	55	31.1, 33.9, 34.7, 36.5, 38.3, 40.1, 41.9, 43.7, 45.5, 47.3, 49.1, 50.9, 52.7, 54.5 (thermocouples)
FLOSSII	5	30	5, 10, 15, 20, 30 (thermistors)
Microfronts	3	10	3, 5, 7, 10 (thermistors)

by snow. We do not analyse flux measurements made in the wind directions between 322.5° and 97.5° to eliminate flow through the tower.

(*c*) *Microfronts*

The Microfronts field study was carried out in rangeland in south central Kansas, USA in March 1995. Micrometeorological measurements were made in two tower groups. The present study analyses data from the more homogeneous south-tower cluster. The south-tower cluster consisted of three 10 m towers separated by 10 m in a line from direction north-east to south-west. The first tower was instrumented with sonic anemometers (ATI K-probe) at 3 and 10 m height. The sampling rate of the sonic anemometers was 10 Hz. The second tower was equipped with propeller-vane anemometers operating at 5 Hz for wind direction and speed at 3, 5 and 10 m. On the third tower, air temperature was sampled at 1 Hz at 5 levels (2, 3, 5, 7 and 10 m). Sonic anemometer data obtained between the wind attack angles of 337.5° and 112.5° are eliminated because of flow through the tower. More details of this experiment can be found in Howell and Sun (1999). All the data are quality-controlled according to Vickers and Mahrt (1997).

4. VERTICALLY INTEGRATED HEAT BUDGET

Table 1 summarizes the heights and depths of layers for the heat budget analysis. For CASES-99 and FLOSSII, we do not include the layer below 5 m because of possible loss of flux due to path-length averaging (see appendix C) and because of possibly large radiative-flux divergence at the surface that is difficult to estimate. For the CASES-99 60 m tower, the heat budget is analysed separately for the lower and upper parts of the tower (Table 1). The vertical heat flux often decreased monotonically with height and vanished between 20 and 30 m above the ground (Mahrt and Vickers 2002), whereas turbulence in the upper part of the tower layer often appeared to be associated with a low-level jet (Banta *et al.* 2002).

To identify the period of stable boundary layers for each field program, we composited the vertical heat flux for the levels at the top and bottom of the layers as a function of the time of day. The first and last hours of the nocturnal period with downward heat flux are discarded to reduce non-stationarity associated with the transitions.

The remaining hours considered for the heat budget analysis are 1800–0700, 1700–0800 and 1900–0700 LST (LST = UTC −6 h) for CASES-99, FLOSSII and Microfronts, respectively. To exclude mesoscale motions from the turbulent part of the flow, we allow τ to vary between records based on the co-spectra of vertical sensible-heat flux (Vickers and Mahrt 2006). The averaging time τ decreases to time-scales as small as a few seconds for very stable conditions. Fluxes are then averaged over $\tau_F = 1$ hour.

Boundary-layer budgets of heat and other quantities are sometimes evaluated in terms of volumetric budgets using aircraft data (Betts *et al.* 1990; Sun *et al.* 1998). Our tower datasets are more applicable to vertically integrated budgets. Vertical integration of Eq. (7) yields

$$\begin{aligned}\int_{z_1}^{z_2} \frac{\partial[\theta]}{\partial t}\,\mathrm{d}z = &- \int_{z_1}^{z_2} [\mathbf{V}_\mathrm{H}]\cdot\nabla[\theta]\,\mathrm{d}z - \int_{z_1}^{z_2} [\mathbf{W}]\frac{\partial[\theta]}{\partial z}\,\mathrm{d}z \\ &- \int_{z_1}^{z_2}\left(\frac{\partial[\overline{u'\theta'}]}{\partial x} + \frac{\partial[\overline{v'\theta'}]}{\partial y}\right)\mathrm{d}z - \int_{z_1}^{z_2}\frac{\partial[\overline{w'\theta'}]}{\partial z}\,\mathrm{d}z \\ &- \int_{z_1}^{z_2}\left(\frac{\partial[u^*\theta^*]}{\partial x} + \frac{\partial[v^*\theta^*]}{\partial y}\right)\mathrm{d}z - \int_{z_1}^{z_2}\frac{\partial[w^*\theta^*]}{\partial z}\,\mathrm{d}z \\ &- \int_{z_1}^{z_2}\frac{1}{\rho c_p}\frac{\partial[F_n]}{\partial z}\,\mathrm{d}z,\end{aligned} \tag{8}$$

where z_1 and z_2 indicate the lower and upper levels of the air layer. Liquid water was never present in any of the layers, so that the heat of phase change of water is neglected.

(*a*) *Temperature tendency, vertical heat-flux divergence and residual*

The layer-integrated potential temperature is computed by first linearly interpolating the discrete measurements of potential temperature (Table 1). In the first method for estimating the tendency, the layer-integrated potential temperature is linearly regressed on time for every hour. The values at the beginning and end of the hour are calculated from the estimated regression line. In the second method, the vertically integrated potential temperature at the beginning and end of the hour is computed by averaging over 10 min windows centred at the boundaries. For evaluation of the heat budget, the tendency term is set to the mean of the tendency estimated by the two methods.

The vertical heat-flux divergence term is evaluated from the hourly average of the turbulence heat flux. The residual R for the evaluated heat budget is defined as

$$\begin{aligned}\int_{z_1}^{z_2}[R]\,\mathrm{d}z &\equiv -\left(\int_{z_1}^{z_2}\frac{\partial[\theta]}{\partial t}\,\mathrm{d}z + \int_{z_1}^{z_2}\frac{\partial[\overline{w'\theta'}]}{\partial z}\,\mathrm{d}z\right) \\ &= -\int_{z_1}^{z_2}\frac{\partial[\theta]}{\partial t}\,\mathrm{d}z - ([\overline{w'\theta'}]_{z_2} - [\overline{w'\theta'}]_{z_1}).\end{aligned} \tag{9}$$

Numerical estimates of individual terms in Eq. (8) and the residual, $\int_{z_1}^{z_2}[R]\,\mathrm{d}z$, are hereafter reported in terms of the mean-layer values (operator: $\langle\,\rangle \equiv (z_2 - z_1)^{-1}$).

$$\left.\begin{aligned}\langle H\rangle &\equiv \left([\overline{w'\theta'}]_{z_2} - [\overline{w'\theta'}]_{z_1}\right)\Big/(z_2 - z_1), \\ \langle T\rangle &\equiv \left(\int_{z_1}^{z_2}\frac{\partial[\theta]}{\partial t}\,\mathrm{d}z\right)\Big/(z_2 - z_1), \\ \langle R\rangle &\equiv \left(\int_{z_1}^{z_2}[R]\,\mathrm{d}z\right)\Big/(z_2 - z_1).\end{aligned}\right\} \tag{10}$$

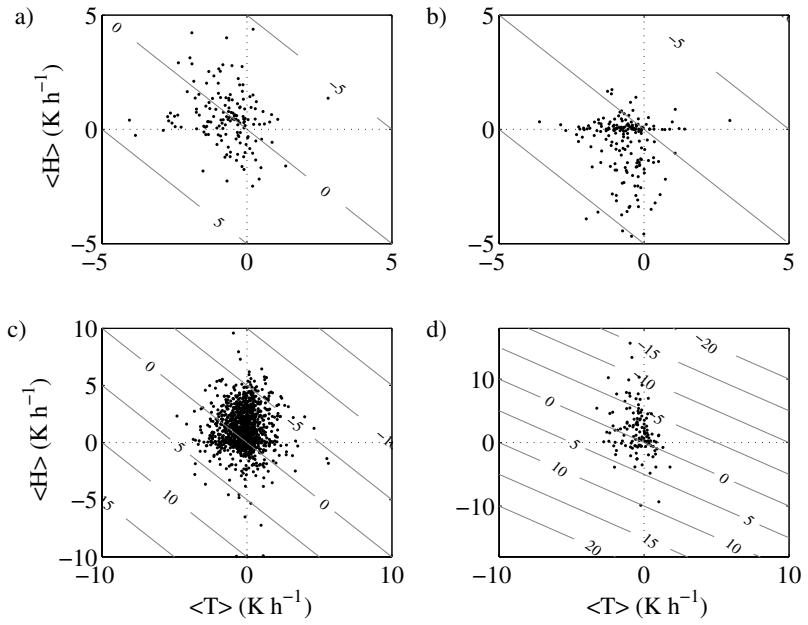

Figure 2. Joint distribution of the vertical heat-flux divergence term, $\langle H \rangle$ and the tendency term, $\langle T \rangle$ (Eq. (10)) for individual hourly records for (a) CASES-99 lower layer, (b) CASES-99 upper layer, (c) FLOSSII, and (d) Microfronts. Contour lines (interval = 5 K h^{-1}) indicate the residual of the heat budget $\langle R \rangle$.

The tendency, vertical heat-flux divergence and residual evaluated for individual hourly records are illustrated in Fig. 2.

(*b*) *Field experiment averages*

The characteristics of the temperature tendency, vertical heat-flux divergence and residual terms for the entire experiment, are examined in terms of the constancy of a given term X defined as

$$\text{constancy} \equiv 1/N \sum_{i=1}^{N} X_i \Big/ \frac{1}{N} \sum_{i=1}^{N} |X_i|, \tag{11}$$

where N indicates the number of hourly records, and where X is either $\int_{z_1}^{z_2} (\partial[\theta]/\partial t)\, \mathrm{d}z$, $\int_{z_1}^{z_2} (\partial[\overline{w'\theta'}]/\partial z)\, \mathrm{d}z$ or $\int_{z_1}^{z_2} [R]\, \mathrm{d}z$ for the record i. In the hypothetical limit, when X occurs randomly with either sign, the constancy is 0. When the term X is positive (negative) for all the records, the constancy is 1 (-1). The advantage of this parameter will become clear in the discussion of the results below. Figures 3–5 summarize the numerator and denominator of Eq. (11) and the constancy computed for each layer. The experiment-averaged tendency term is negative for all the datasets although it is small for FLOSSII where warming events were frequently observed. That is, the sign of the tendency term is less systematic between records for FLOSSII than the other datasets.

For the CASES-99 lower layer, FLOSSII and Microfronts, the observed cooling is the same sign as predicted by the flux divergence, i.e. the heat-flux divergence contributes to the cooling of the air in agreement with the concept of a nocturnal boundary layer. In contrast, the flux divergence term is convergent with large constancy for the CASES-99 upper layer. The increasing downward heat flux with height for this

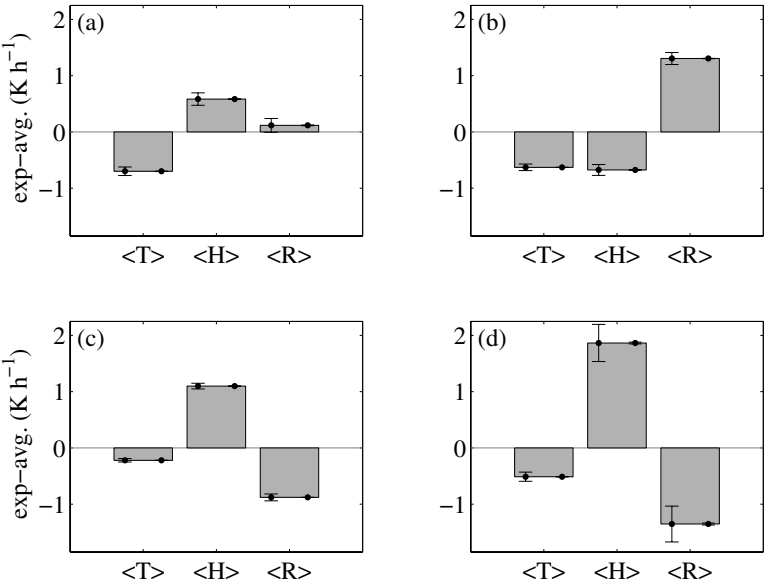

Figure 3. The temperature tendency $\langle T \rangle$, vertical heat-flux divergence $\langle H \rangle$ and residual $\langle R \rangle$ averaged over the entire experiment: (a) CASES-99 lower layer, (b) CASES-99 upper layer, (c) FLOSSII and (d) Microfronts. The error bar on the left of each bar is the 'standard error' of the experiment-averaged value. The error bar on the right is the experiment-averaged $\langle \mathrm{Err}_T \rangle$, $\langle \mathrm{Err}_H \rangle$ or $\langle \mathrm{Err}_R \rangle$ (see appendix B).

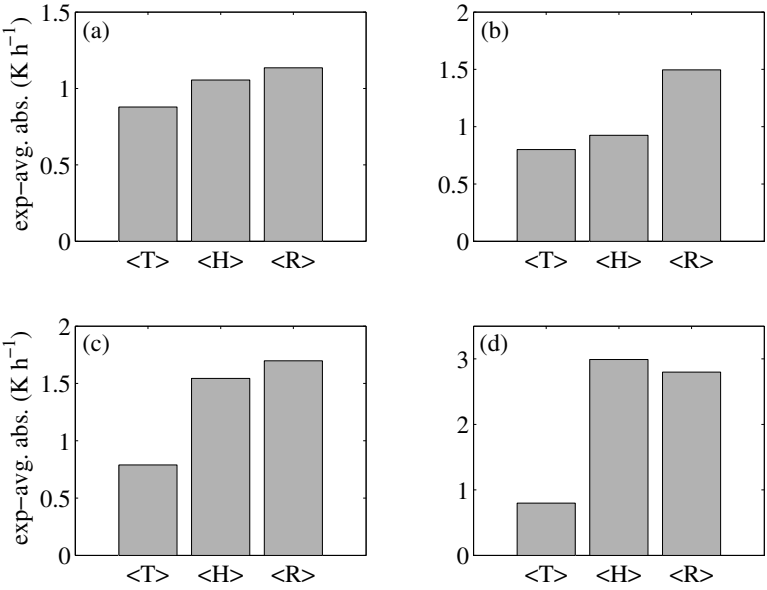

Figure 4. Same as Fig. 3 except for the experiment average of the absolute values of the temperature tendency $\langle T \rangle$, vertical heat-flux divergence $\langle H \rangle$ and residual $\langle R \rangle$.

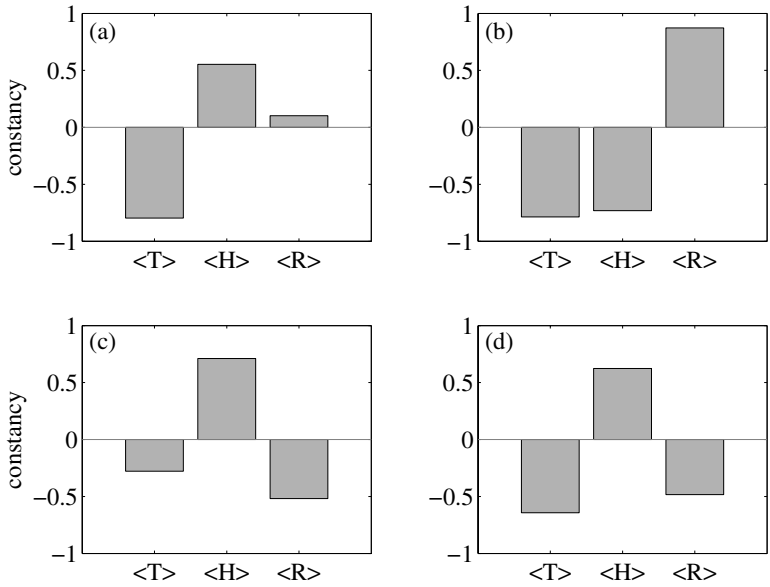

Figure 5. Constancy of the temperature tendency $\langle T \rangle$, vertical heat-flux divergence $\langle H \rangle$ and residual $\langle R \rangle$.

layer is thought to be associated with shear-generated turbulence on the underside of the low-level jet (Banta *et al.* 2002). However, the tendency term for the upper layer is on average negative (cooling). Since the heat-flux convergence predicts warming, the observed cooling must be due to the other unevaluated terms in the heat budget (section 5(a)–(d)) or systematic observational errors (appendix B).

The experiment average of the residual is small for the CASES-99 lower layer. However, a small experiment average of the residual does not necessarily imply that the temperature tendency and heat-flux divergence are in balance for individual records. Figure 4 suggests that the residual for individual hourly records is large for all field programs. Therefore, the small experiment-averaged residual for the CASES-99 lower layer is a consequence of averaging primarily random residual with no obvious sign preference. On the other hand, the experiment-averaged residuals for the CASES-99 upper layer, FLOSSII and Microfronts are more systematic, implying important systematic observational errors or systematic contributions from other terms such as temperature advection.

5. Sources of the residual

In this section, the full heat budget is examined to identify sources of the observed large residual. Uncertainties associated with (i) the estimated tendency due to the calculation methods and (ii) the vertical heat-flux divergence due to random sampling errors are generally small compared to the residual (appendix B). While we cannot completely rule out problems with instrumentation as a source of the residual, it is unlikely that the large residuals can be explained by sampling and instrumentation problems alone (appendix C). We now estimate the horizontal heat-flux divergence, radiative-flux divergence, temperature advection and mesoscale flux divergence terms.

(*a*) *Horizontal divergence of the turbulence heat flux*

The order of magnitude of the horizontal divergence of turbulence heat flux,

$$\int_{z_1}^{z_2} \left(\frac{\partial[\overline{u'\theta'}]}{\partial x} + \frac{\partial[\overline{v'\theta'}]}{\partial y} \right) \mathrm{d}z,$$

is estimated from the 5 m turbulence measurements at the six satellite towers within the CASES-99 tower network (section 3). The horizontal heat-flux divergence is estimated for the main tower 5 m level using the linear vector point function method (LVPF) (Zamora *et al.* 1987). This method requires three-point measurements of a variable (e.g. horizontal heat flux) and assumes that the variable increases or decreases linearly on a two-dimensional triangular plane coincident with the measurement points. This analysis is first performed using horizontal heat-flux measurements on the 100 m radius and is repeated using those on the 300 m radius. Flux data are available at all 5 m levels of the tower network for only 87 of 153 hours for which the heat budget analysis is performed for the CASES-99 lower layer (Table B.1).

The horizontal heat-flux divergence term for the one-hour records is generally on the order of a few tenths of a degree per hour or less, but occasionally becomes close to ± 1 K h^{-1}. The sign of this term frequently switches from one record to another as indicated by the constancy of only -0.13 and 0.44 for the 100 and 300 m radii, respectively. While these results suggest the potential importance of the horizontal heat-flux divergence in the hourly heat budget, the reported values of this term should be interpreted with caution because of possibly large random errors for individual records. The experiment-averaged horizontal heat fluxes mapped across the CASES-99 tower network are spatially coherent, but yield a value of the horizontal heat-flux divergence on the order of only 0.01 K h^{-1}, which is negligible in the experiment-averaged heat budget.

(*b*) *Radiative-flux divergence*

No adequate radiation measurements are available for estimating the radiative-flux divergence,

$$\int_{z_1}^{z_2} \frac{1}{\rho c_p} \frac{\partial[F_n]}{\partial z} \, \mathrm{d}z,$$

across the air layers in Table 1. Based on CASES-99 tower radiation measurements, Sun *et al.* (2003) estimated radiative-flux divergence for a deeper layer of 2–48 m and found that the radiative-flux divergence typically becomes largest in the early evening. The monthly mean of the radiative-flux divergence in the early evening for their air layer was on the order of a few tenths of a degree per hour, although they reported values as high as ~ 1 K h^{-1} for one of the early evening periods. The experiment-averaged radiative-flux divergence became close to zero for the rest of the night.

The modelling study of Ha and Mahrt (2003) also concluded that the radiative-flux divergence becomes large in the early evening and can be the primary contributor to the initial formation of the surface inversion in CASES-99. In the early evening, the radiative-flux divergence was typically ~ 0.5 K h^{-1} for the 60 m tower layer except within a few metres closest to the ground surface, where the cooling rate became 1 to 3 K h^{-1}. However, the model is probably inaccurate close to the ground. Later in the evening, the magnitude of the radiative-flux divergence decreased to half of that in the early evening and became substantially smaller than the vertical heat-flux divergence. Earlier modelling studies (e.g. Garratt and Brost 1981; André and Mahrt 1982; Estournel *et al.* 1986) have estimated similar radiative cooling rates.

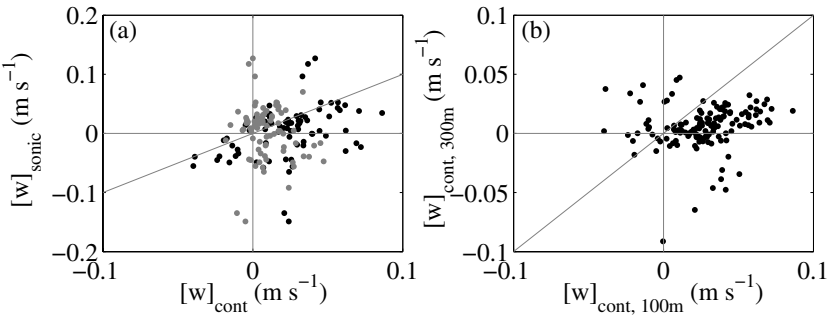

Figure 6. (a) Comparison of [**W**] (see text) estimated from the sonic anemometer and from the continuity equation for the main tower 10 m level in CASES-99. Horizontal divergence is estimated from wind vectors for the 100 m radius (black) and 300 m radius (grey) towers. (b) Comparison of [**W**] computed from the horizontal divergence estimated from wind vectors at 100 and 300 m radius. The diagonal grey lines correspond to 1:1 lines.

Based on these values, we estimate the typical radiative-flux divergence to be to a few tenths of a degree per hour for all the air layers investigated in the present study, although this is probably an overestimation for FLOSSII where the moisture content is extremely small. This typical magnitude of the radiative-flux divergence would explain the residual of the records falling between the contour lines of zero and a few tenths of K h^{-1} in Fig. 2. However, inspection of the Fig. 2 reveals that the radiative-flux divergence alone is too small to explain the residual of most of the records and sometimes has the wrong sign to explain the residual. Large residuals did not preferentially occur in the early evening hours, when the radiative-flux divergence could become large, but rather occurred with comparable frequency throughout the night.

(*c*) *Advection*

Evaluation of the vertical advection term requires accurate estimates of the mean vertical motion. Even a small sensor tilt relative to the ground can seriously contaminate the true vertical mean wind speed. For example, an instrument tilt of 1° induces a spurious mean vertical wind velocity [**W**] of 8 cm s^{-1} for a horizontal mean wind speed of 5 m s^{-1}.

The vertical wind velocity [**W**] at the 10 m level on the CASES-99 main tower is estimated with two methods, one directly from the sonic anemometer and the other from the mass continuity equation using estimates of the horizontal divergence of the wind vector. The divergence of horizontal wind, $\nabla \cdot \mathbf{V}_H$, is evaluated at the 5 m level with the LVPF method (section 5(a)). Wind velocity [**W**], at the 10 m level, is evaluated in terms of $\nabla \cdot \mathbf{V}_H$ at 5 m by assuming that $\nabla \cdot \mathbf{V}_H$ increases linearly with height from zero at the ground surface. The values of [**W**] estimated from the continuity equation and the sonic anemometer frequently disagree both in order of magnitude and sign (Fig. 6(a)). Vertical wind [**W**] calculated from the horizontal divergence from the 100 and 300 m radii agree better with each other in magnitude, but even then, one third of the two divergence estimates disagree in sign. While the estimate from the 300 m radius is less vulnerable to small differences between large numbers, the horizontal divergence based on the 100 m radius may be more relevant to the 10 m vertical motions on the tower. Sources of the differences between [**W**] estimates are currently under investigation, and confident estimates of [**W**] are not possible.

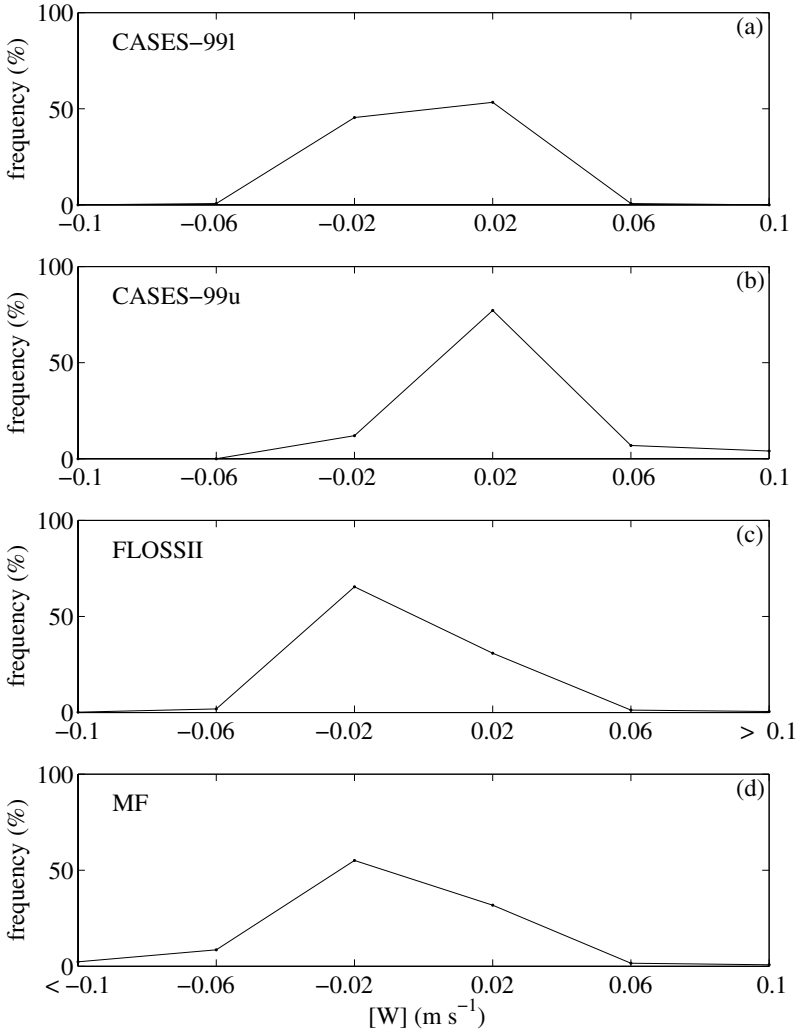

Figure 7. Frequency distribution of the magnitude of [**W**] for (a) CASES-99 lower layer, (b) CASES-99 upper layer, (c) FLOSSII, and (d) Microfronts, estimated from the residual of the heat budget.

As an exercise, we evaluate the order of magnitude of [**W**] required for the entire residual to be balanced by the vertical advection term. The vertical potential-temperature gradient is estimated from finite differencing. For all the sites, most of the records yield an inferred absolute value of the mean layer, [**W**], of less than a few cm s^{-1} (Fig. 7). That is, even a small value of [**W**], probably too small to measure with existing methodologies, could potentially explain the entire residual.

We are unable to estimate the horizontal temperature advection term for the heat budget because none of the present datasets provide adequate air temperature measurements necessary for calculating the horizontal potential-temperature gradients. The horizontal potential-temperature gradient required to balance the heat budget corresponds to potential-temperature difference of only a few hundredths of a degree over a horizontal distance of 100 m for all records for all the sites (not shown), similar to the results of Ha and Mahrt (2003). While such small horizontal potential-temperature gradients can

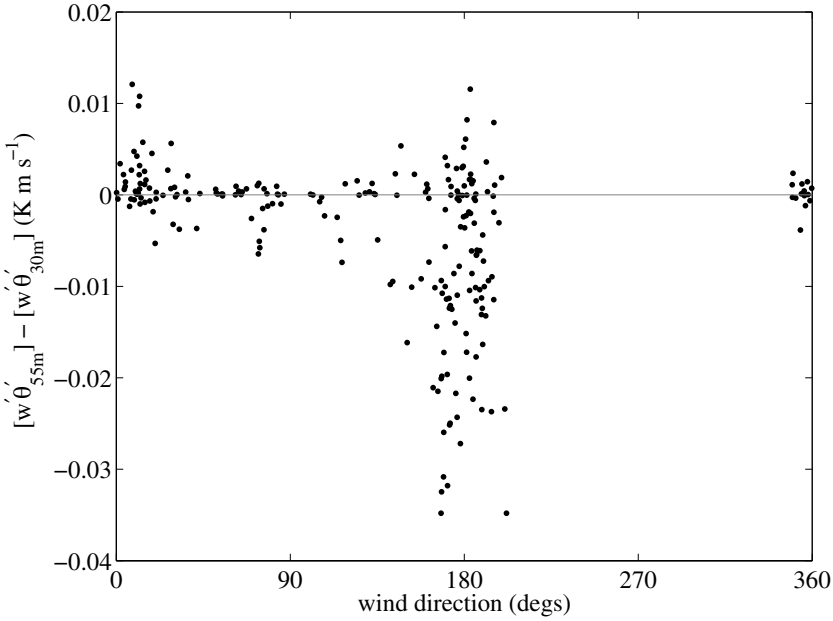

Figure 8. Vertical heat-flux divergence across the CASES-99 upper layer (30–55 m), as a function of wind direction for individual hourly records.

significantly modify the structure of stable boundary layers, they are difficult to measure. Difficulties arise from the random sampling errors for the estimation of the horizontal potential-temperature gradients, limitation in the accuracy of sensors and ambiguity of the standardized measurement height above vegetation of varying height (Nakamura and Mahrt 2005b). Errors for the estimated difference in the surface elevation between two points of sensor deployment are another factor because elevation information is used for computing the potential temperature from the measured air temperature. These errors could yield spurious horizontal potential-temperature gradients that are significant relative to the actual horizontal potential-temperature gradients.

In the heat budget of the CASES-99 upper layer, vertical heat-flux convergence (warming) is frequently observed while the observed tendency term is negative (cooling) (Fig. 2(b)). These cases are observed with southerly wind (Fig. 8). Soler *et al.* (2002) find that cold air, collected in a lower-lying area to the south of the CASES-99 main tower, occasionally mixes upward, sometimes during events of downward transport of turbulence. These observations suggest that cold air advection might explain the imbalance of the hourly heat budget of the CASES-99 upper layer when the negative tendency and vertical heat-flux convergence occur concurrently. The cold air advection could also be due to regional horizontal temperature gradients. The temperature tendency and vertical heat-flux divergence balance reasonably well in the lower layer (Fig. 3) implying that cold air advection is not important. This apparent lack of importance could be due to the fact that the flow in the lower-lying areas is generally northerly (downslope) and becomes southerly only after the mixing eliminates the low-lying cold air (Mahrt *et al.* 2001b). It is also possible that cold air advection could still be significant but balanced by neglected terms and/or systematic errors for the evaluated terms.

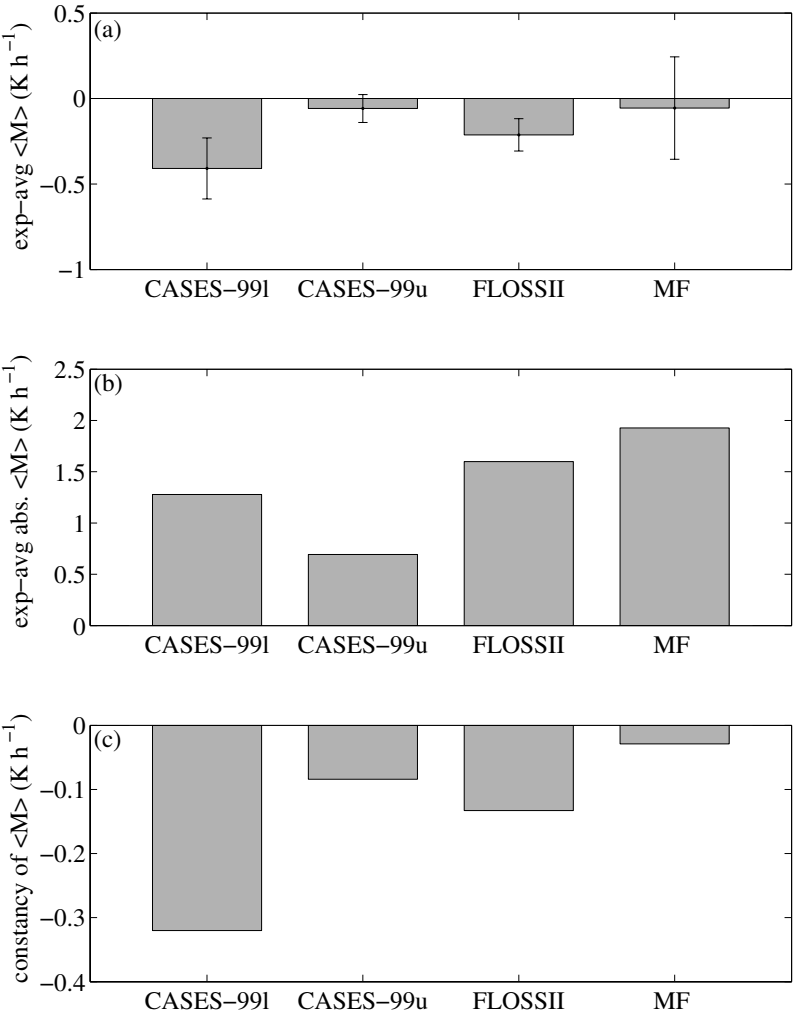

Figure 9. Statistics of the vertical mesoscale heat flux divergence $\langle M \rangle$ for CASES-99 lower layer, CASES-99 upper layer, FLOSSII and Microfronts: (a) the experiment-average of $\langle M \rangle$, (b) the experiment-average of the absolute value of $\langle M \rangle$, and (c) constancy of $\langle M \rangle$. Error bars in (a) indicate the 'standard error' of the experiment-average of $\langle M \rangle$.

(*d*) *Mesoscale heat-flux divergence*

Because the hourly average of the mesoscale heat flux is subject to large random sampling errors, such estimates are inadequate even as a rough estimate of the ensemble-averaged mesoscale flux (Vickers and Mahrt 2006). Therefore, the potential significance of the vertical mesoscale heat-flux divergence,

$$\int_{z_1}^{z_2} \frac{\partial [w^* \theta^*]}{\partial z} \, \mathrm{d}z,$$

is examined by averaging $[w^* \theta^*]$ from individual one-hour records over the entire field experiment (Fig. 9).

$$\langle M \rangle \equiv \frac{[w^* \theta^*]_{z_2} - [w^* \theta^*]_{z_1}}{z_2 - z_1}. \tag{12}$$

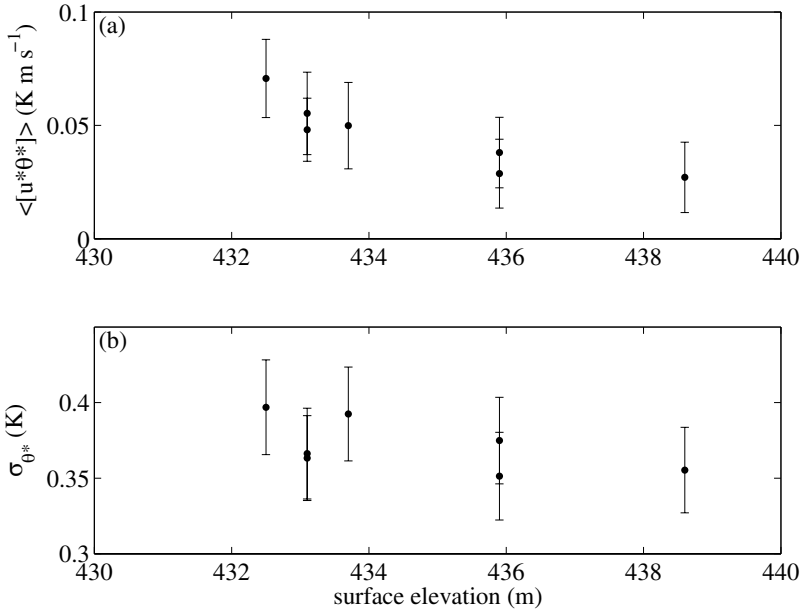

Figure 10. (a) Experiment-averaged along-wind mesoscale horizontal heat flux at 5 m as a function of surface elevation with standard errors over 87 records at individual towers. (b) Experiment-averaged standard deviation σ_{θ^*} at 5 m as a function of surface elevation.

The constancy of the mesoscale vertical heat-flux divergence for the experiment is relatively small depending on site, probably due to transient mesoscale motions. Nonetheless, the experiment average of the vertical divergence of the mesoscale heat flux is larger than its 'standard error' for the CASES-99 lower layer and FLOSSII. However, the experiment-averaged mesoscale vertical heat-flux divergence is too small or has the wrong sign to explain the experiment-averaged residual, depending on the site.

The divergence of the mesoscale horizontal heat flux,

$$\int_{z1}^{z2} \left(\frac{\partial [u^* \theta^*]}{\partial x} + \frac{\partial [v^* \theta^*]}{\partial y} \right) \mathrm{d}z,$$

is estimated for 87 out of 153 hours for which the heat budget is analysed for the CASES-99 lower layer (section 5(a)). The along-wind mesoscale horizontal heat flux is positive (Fig. 10(a)), consistent with the stable stratification, i.e. greater (smaller) horizontal momentum is associated with sinking (rising) air. The experiment-averaged values of mesoscale horizontal heat flux for the CASES-99 tower network does not show obvious spatial coherence.

However, the positive experiment-averaged mesoscale heat flux decreases systematically with increasing surface elevation (Fig. 10(a)) in spite of the small variation of surface elevation of only 6 m over the horizontal distance of 400 m. The observed relationship between the mesoscale horizontal heat flux and elevation may be explained by increasing vertical potential-temperature gradient with decreasing elevation, possibly due to modest pooling of cold air. This speculation is supported by generally increasing standard deviation of the 5 m mesoscale temperature fluctuations θ^* with decreasing surface elevation (Fig. 10(b)).

Figure 10(a) indicates that the mesoscale horizontal heat-flux divergence is potentially significant in the experiment-averaged heat budget. For example, based on the

values of the experiment-averaged mesoscale flux from the towers at the lowest and highest surface elevations, we tentatively estimate the mesoscale horizontal heat-flux divergence to be 0.5 K h^{-1}.

6. Conclusions

The stable nocturnal boundary layer is commonly viewed as a balance between the temperature tendency and vertical heat-flux divergence. The validity of this assumption has been examined by analysing data from three field programs. Observed cooling/warming (tendency term) approximately balances the vertical heat-flux divergence with confidence for only a small fraction of one-hour records (section 4(a)). In the rest of the records, the observed tendency was either much too small or much too large or even the wrong sign to balance the vertical heat-flux divergence. Our analysis indicates that uncertainties associated with the tendency and vertical heat-flux divergence are small compared to the residual of the two-term balance. Although instrumentation errors cannot be completely eliminated as a significant source of the residual, our error analysis implies that the large residual cannot be explained by instrumentation errors alone.

While no direct estimates of radiative-flux divergence are possible from the available data, the residual of the heat budget generally substantially exceeds typical values of the radiative-flux divergence reported in the literature or based on a radiation model applied to CASES-99 data. Based on the CASES-99 dataset, the magnitude of the horizontal heat-flux divergence is also too small to explain the residual. Circumstantial evidence at one site indicates that advection of temperature may explain much of the residual.

The analysis in section 5(c) indicates that the horizontal gradient of potential temperature and the mean vertical velocity, and therefore advection, cannot be confidently estimated. The mesoscale heat-flux divergence may be significant in the heat budget, although reliable estimates of these terms also require improved observational strategies. In terms of the heat budget and associated vertical structure of the nocturnal boundary layer, additional fieldwork with existing strategies and technologies will fail. Even weak surface heterogeneity may induce important horizontal variations in the very stable boundary layer, and new approaches for measuring horizontal variation of temperature and fluxes are required.

Acknowledgements

We gratefully acknowledge the comments and data processing assistance of Dean Vickers and the collection of the eddy-correlation data for all three sites by the Atmospheric Technology Division of the National Center for Atmospheric Research. We also wish to thank Tsutomu Watanabe and two anonymous reviewers for their helpful comments to improve the original manuscript. This work is supported by the NASA Headquarters under the Earth System Science Fellowship Grant NGT5-30387, the Physical Meteorology Program of the National Science Foundation under grant ATM-0107617 and the Army Research Office under grant DAAD19-02-1-0224.

Appendix A

Significance of the residual

(i) *Error estimates of the tendency term.* The temperature tendency term for one-hour records was estimated by (i) fitting a linear regression line to the time dependence of the

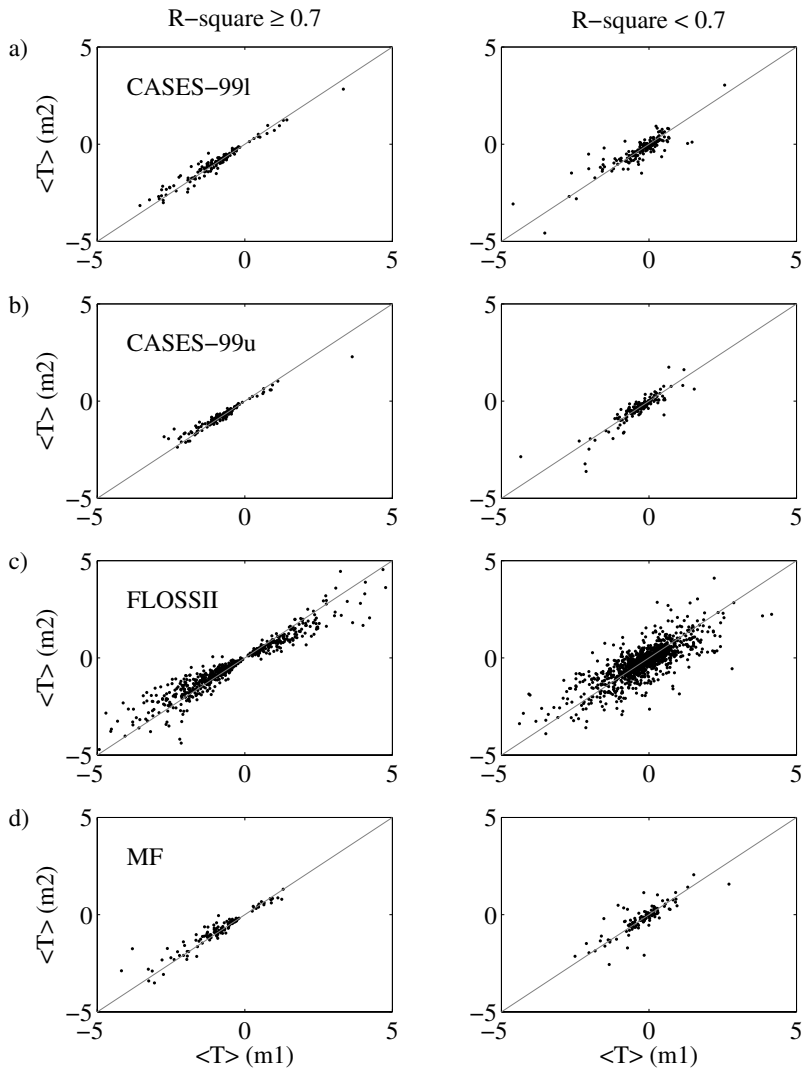

Figure A.1. Comparison of the mean-layer temperature tendency $\langle T \rangle$ (K h^{-1}) estimated by two methods for: (a) CASES-99 lower layer, (b) CASES-99 upper layer, (c) FLOSSII, and (d) Microfronts. The first (second) method are indicated by subscript m1 (m2). The left (right) column represents the high (low) $\geq$0.7 ($<$0.7) R-square values for the linear regression for the first method. Grey lines indicate 1:1 lines.

vertically integrated potential temperature, and (ii) averaging the vertically integrated potential temperature over 10 min windows centred at the beginning and the end boundaries of the record (section 4(a)). The disagreement between the two methods is relatively small and is approximately random, except for FLOSSII high R-square hours for the regression lines (Fig. A.1) where the first method tends to yield a larger value in magnitude than the second method. The records with the largest differences were associated with mesoscale fronts which were frequently observed across the region.

A measure of the uncertainty of the estimated tendency term, Err_T, is defined as

$$\mathrm{Err}_T = \frac{1}{2}\left| \int_{z_1}^{z_2} \frac{\partial[\theta]}{\partial t}\, \mathrm{d}z_{\mathrm{m1}} - \int_{z_1}^{z_2} \frac{\partial[\theta]}{\partial t}\, \mathrm{d}z_{\mathrm{m2}} \right|, \tag{A.1}$$

where $\int_{z_1}^{z_2}(\partial[\theta]/\partial t)\,\mathrm{d}z_{\mathrm{m1}}$ and $\int_{z_1}^{z_2}(\partial[\theta]/\partial t)\,\mathrm{d}z_{\mathrm{m2}}$ indicate the tendency term estimated by the first and second methods, respectively.

(ii) *Error estimates of the vertical heat-flux divergence term.* The error of the computed vertical heat-flux divergence, Err_H, is estimated as

$$\mathrm{Err}_H = \mathrm{RSE}_{H-\mathrm{u}} + \mathrm{RSE}_{H-\mathrm{l}}, \tag{A.2}$$

where $\mathrm{RSE}_{H-\mathrm{u}}$ and $\mathrm{RSE}_{H-\mathrm{l}}$ indicate random sampling errors of vertical heat flux at upper and lower levels of an air layer, respectively. The random sampling errors of the vertical heat flux at an observational height can be estimated as

$$\mathrm{RSE}_H = \frac{\sigma_{\overline{w'\theta'}}}{n^{1/2}}, \tag{A.3}$$

where $\sigma_{\overline{w'\theta'}}$ and n indicate the standard deviation of sub-record vertical heat fluxes and the number of sub-record fluxes, respectively. The error Err_H in Eq. (A.2) is generally an overestimate of the random error for the heat-flux divergence estimate since it ignores sign differences between the two terms on the right-hand side.

APPENDIX B

Error estimates and significance of the residual

Uncertainty of the estimated residual, Err_R, due to the uncertainties of the terms on the right-hand side of Eq. (9), is estimated as

$$\mathrm{Err}_R \equiv \mathrm{Err}_T + \mathrm{Err}_H. \tag{B.1}$$

This error estimate for the residual, Err_R, is also an overestimate because it assumes the errors on the right-hand side always have the same sign. For examining the significance of the residual, two criteria are introduced. First, if the absolute magnitude of the residual for individual records is larger than the error Err_R, we consider the residual to be statistically significant. Second, if the ratio of the absolute value of the residual to the absolute value of the tendency fulfils the relationship

$$\left|\int_{z_1}^{z_2} R\,\mathrm{d}z\right| \Big/ \left|\int_{z_1}^{z_2} \frac{\partial[\theta]}{\partial t}\,\mathrm{d}z\right| > \alpha, \tag{B.2}$$

the magnitude of the residual is considered significant for explaining the observed temperature tendency in the heat budget. Table B.1 summarizes the result of the two-step significance analysis with $\alpha = 0.5$ and 1 for the second test. The percentage of the entire records in which the computed residual fulfils both of the significance criteria varies between 49–80% and 40–59% of the records for $\alpha = 0.5$ and $\alpha = 1.0$, respectively, depending on the dataset (Table B.1). This result suggests that the residual corresponds to a significant portion of the heat budget in many of the records.

APPENDIX C

Instrumentation problems

Use of sonic anemometers of different designs at different heights in CASES-99 may induce systematic bias in the estimated vertical heat-flux divergence. However, the composite of the vertical profile of turbulence vertical heat fluxes over the entire experimental period is smooth with no obvious bias at individual heights.

TABLE B.1. SUMMARY OF THE SIGNIFICANCE TESTS OF THE HOURLY RESIDUAL. SECOND COLUMN: TOTAL HOURS FOR WHICH THE LAYER HEAT BUDGET ANALYSIS IS PERFORMED. THIRD COLUMN: PERCENTAGE OF TOTAL HOURS FOR WHICH THE RESIDUAL FAILS THE FIRST SIGNIFICANCE TEST (i.e. $|\int_{z_1}^{z_2} R\,\mathrm{d}z| < \mathrm{Err}_R$). FOURTH COLUMN: THRESHOLD OF α APPLIED IN THE SECOND SIGNIFICANCE TEST. FIFTH COLUMN: PERCENTAGE OF TOTAL HOURS FOR WHICH THE RESIDUAL PASSES THE FIRST TEST. SIXTH COLUMN: PERCENTAGE OF TOTAL HOURS FOR WHICH THE RESIDUAL PASSES BOTH SIGNIFICANCE TESTS (SEE TEXT).

Field experiment	Total hours	Failed test 1	Threshold α for test 1	Passed test 1 only	Passed tests 1 and 2
CASES-99 (lower)	153	45%	0.5	5%	50%
			1.0	15%	40%
CASES-99 (upper)	188	11%	0.5	9%	80%
			1.0	30%	59%
FLOSSII	1303	32%	0.5	6%	62%
			1.0	16%	52%
Microfronts	129	46%	0.5	5%	49%
			1.0	9%	45%

Sonic anemometers are unable to capture turbulence motions with length-scales on the order of the path length or smaller. Path-length averaging underestimates the turbulence flux close to the ground where the transporting eddies are small. Based on the comparison of flux estimates by sonic and hot-film anemometers (Skelly *et al.* (2002) and our own such comparisons (unpublished)), we suspect that flux loss due to the path-length averaging is significant below 2 m height.

APPENDIX D

Symbols

c_p	Specific heat at constant pressure
F_n	Net long-wave radiative flux
N	Number of hourly records
R	Residual
u, v, w	Wind velocity components
$\mathbf{V}_\mathrm{H}$	Mean horizontal wind vector
$\mathbf{W}$	Mean vertical motion
x, y, z	Along-wind, cross-wind and vertical coordinates
θ	Potential temperature
ρ	density of dry air
σ	Standard deviation
τ_F	Time-scale of turbulence fluctuations
ϕ	Arbitrary variable

REFERENCES

André, J. C. and Mahrt, L. 1982 The nocturnal surface inversion and influence of clear-air radiative cooling. *J. Atmos. Sci.*, **39,** 864–878

Anfossi, D., Bacci, P. and Longhetto, A. 1976 Forecasting of vertical temperature profiles in the atmosphere during nocturnal radiation inversions from air temperature trend at screen height. *Q. J. R. Meteorol. Soc.*, **102,** 173–180

Banta, R. M., Newsom, R. K., Lundquist, J. K., Pichugina, Y. L., Coulter, R. L. and Mahrt, L. 2002 Nocturnal low-level jet characteristics over Kansas during CASES-99. *Boundary-Layer Meteorol.*, **105,** 221–252

Betts, A. K., Desjardnis, R. L., MacPherson, J. I. and Kelly, R. D. 1990 Boundary-layer heat and moisture budgets from FIFE. *Boundary-Layer Meteorol.*, **50,** 109–138

Brost, R. A. and Wyngaard, J. C. 1978 A model study of the stably stratified planetary boundary layer. *J. Atmos. Sci.*, **35,** 1427–1440

Brunt, D. 1939 *Physical and dynamical meteorology*, second edition. Cambridge University Press

Caughey, S. J., Wyngaard, J. C. and Kaimal, J. C. 1979 Turbulence in the evolving stable boundary layer. *J. Atmos. Sci.*, **36,** 1041–1052

Chimonas, G. 1999 Steps, waves and turbulence in the stable stratified planetary boundary layer. *Boundary-Layer Meteorol.*, **90,** 397–421

Coulter, R. L. and Doran, J. C. 2002 Spatial and temporal occurrences of intermittent turbulence during CASES-99. *Boundary-Layer Meteorol.*, **105,** 329–349

Cuxart, J., Yagüe, C., Morales, G., Terradellas, E., Orbe, J., Calvo, J., Fernández, A., Soler, M. R., Infante, C., Buenestado, P., Espinalt, A., Joergensen, H. E., Rees, J. M., Vilà, J., Redondo, J. M., Cantalapiedra, I. R. and Conangla, L. 2000 Stable atmospheric boundary-layer experiment in Spain (SABLES 98): A report. *Boundary-Layer Meteorol.*, **96,** 337–370

Derbyshire, S. H. 1999 Boundary-layer decoupling over cold surfaces as a physical boundary-instability. *Boundary-Layer Meteorol.*, **90,** 297–325

Estournel, C., Vehil, R. and Guedalia, D. 1986 An observational study of radiative and turbulent cooling in the nocturnal boundary layer (ECLASTS experiment). *Boundary-Layer Meteorol.*, **34,** 55–62

Finnigan, J. J., Clement, R., Malhi, Y., Leunning, R. and Cleugh, H. A. 2003 A re-evaluation of long-term flux measurement techniques Part I: Averaging and coordinate rotation. *Boundary-Layer Meteorol.*, **107,** 1–48

Forrer, J. and Rotach, M. W. 1997 On the turbulence structure in the stable boundary layer over the greenland ice sheet. *Boundary-Layer Meteorol.*, **85,** 111–136

Gage, K. S. 1979 Evidence for a $k^{-5/3}$ law inertial range in mesoscale two-dimensional turbulence. *J. Atmos. Sci.*, **36,** 1950–1954

Garratt, J. R. and Brost, R. A. 1981 Radiative cooling effects within and above the nocturnal boundary layer. *J. Atmos. Sci.*, **38,** 2730–2746

Ha, K.-J. and Mahrt, L. 2003 Radiative and turbulent fluxes in the nocturnal boundary layer. *Tellus*, **55A,** 317–327

Holtslag, A. A. M. and Nieuwstadt, F. T. M. 1986 Scaling the atmospheric boundary layer. *Boundary-Layer Meteorol.*, **36,** 201–209

Howell, J. F. and Sun, J. 1999 Surface-layer fluxes in stable conditions. *Boundary-Layer Meteorol.*, **90,** 495–520

Lilly, D. K. 1983 Stratified turbulence and the mesoscale variability of the atmosphere. *J. Atmos. Sci.*, **40,** 749–761

Lundquist, J. K. 2003 Intermittent and elliptical inertial oscillations in the atmospheric boundary layer. *J. Atmos. Sci.*, **60,** 2661–2673

Mahrt, L. and Vickers, D. 2002 Contrasting vertical structures of nocturnal boundary layers. *Boundary-Layer Meteorol.*, **105,** 351–363

2005 Moisture flux over snow with and without protruding vegetation. *Q. J. R. Meteorol. Soc.*, **131,** 1251–1270

Mahrt, L., Moore, E., Vickers, D. and Jensen, N. O. 2001a Dependence of turbulent and mesoscale velocity variances on scale and stability. *J. Appl. Meteorol.*, **40,** 628–641

Mahrt, L., Vickers, D., Nakamura, R., Soler, M. R., Sun, J., Burns, S. and Lenschow, D. H. 2001b Shallow drainage flows. *Boundary-Layer Meteorol.*, **101,** 243–260

Moraes, O. L. L., Acevedo, O. C., Da Silva, R., Magnago, R. and Siqueira, A. C. 2004 Nocturnal surface-layer characteristics at the bottom of a valley. *Boundary-Layer Meteorol.*, **112,** 159–177

Nakamura, R. and Mahrt, L. 2005a A study of intermittent turbulence with CASES99 tower measurements. *Boundary-Layer Meteorol.*, **114,** 368–387

Nakamura, R. and Mahrt, L. 2005b Air temperature measurement errors in naturally ventilated radiation shields. *J. Atmos. Oceanic Technol.*, **22,** 1046–1058

Nieuwstadt, F. T. M. 1980 A rate equation for the inversion height in a nocturnal boundary layer. *J. Appl. Meteorol.*, **19,** 1445–1447

1984 The turbulent structure of the stable nocturnal boundary layer. *J. Atmos. Sci.*, **41,** 2202–2216

Poulos, G. S., Blumen, W., Fritts, D. C., Lundquist, J. K., Sun, J., Burns, S. P., Nappo, C., Banta, R., Newsom, R., Cuxart, J., Terradellas, E., Balsley, B. and Jensen, M. 2002 CASES-99: A comprehensive investigation of the stable nocturnal boundary layer. *Bull. Am. Meteorol. Soc.*, **83,** 555–581

Salmond, J. A. 2005 Wavelet analysis of intermittent turbulence in a very stable nocturnal boundary layer: Implications for the vertical mixing of ozone. *Boundary-Layer Meteorol.*, **114,** 463–488

Skelly, B. T., Miller, D. R. and Meyer, T. H. 2002 Triple-hot-film anemometer performance in CASES-99 and a comparison with sonic anemometer measurements. *Boundary-Layer Meteorol.*, **105,** 275–304

Smedman, A.-S. 1988 Observations of a multi-level turbulence structure in a very stable atmospheric boundary layer. *Boundary-Layer Meteorol.*, **44,** 231–253

Soler, M. R., Infante, C., Buenestado, P. and Mahrt, L. 2002 Observations of nocturnal drainage flow in a shallow gully. *Boundary-Layer Meteorol.*, **105,** 253–273

Sun, J., Desjardins, R., Mahrt, L. and MacPherson, I. 1998 Transport of carbon dioxide, water vapor and ozone by turbulence and local circulations. *J. Geophys. Res.*, **103,** 25873–25885

Sun, J., Burns, S. P., Lenschow, D. H., Banta, R., Newsom, R., Coulter, R., Frasier, S., Ince, T., Nappo, C., Cuxart, J., Blumen, W., Lee, X. and Hu, X-Z 2002 Intermittent turbulence associated with a density current passage in the stable boundary layer. *Boundary-Layer Meteorol.*, **105,** 199–219

Sun, J., Burns, S. P., Delany, A. C., Oncley, S. P., Horst, T. W. and Lenschow, D. H. 2003 Heat balance in the nocturnal boundary layer during CASES-99. *J. Appl. Meteorol.*, **42,** 1649–1666

Troen, I. and Mahrt, L. 1986 A simple model of the atmospheric boundary layer: Sensitivity to surface evaporation. *Boundary-Layer Meteorol.*, **37,** 129–148

Van de Wiel, B. J. H., Moene, A. F., Ronda, R. J., De Bruin, H. A. R. and Holtslag, A. A. M. 2002 Intermittent turbulence and oscillations in the stable boundary layer over land. Part II: A system dynamics approach. *J. Atmos. Sci.*, **59,** 2567–2581

Vickers, D. and Mahrt, L. 1997 Quality control and flux sampling problems for tower and aircraft data. *J. Atmos. Oceanic Technol.*, **14,** 512–526

2003 The cospectral gap and turbulent flux calculations. *J. Atmos. Oceanic Technol.*, **20,** 660–672

2004 Evaluating formulations of stable boundary layer height. *J. Appl. Meteorol.*, **43,** 1736–1749

2006 A solution for flux contamination by mesoscale motions with very weak turbulence. *Boundary-Layer Meteorol.* (in press)

Zamora, R. J., Shaprio, M. A. and Doswell, C. A. III 1987 The diagnosis of upper tropospheric divergence and ageostrophic wind using profiler wind observations. *Mon. Weather Rev.*, **115,** 871–884